INS-NUMA-34

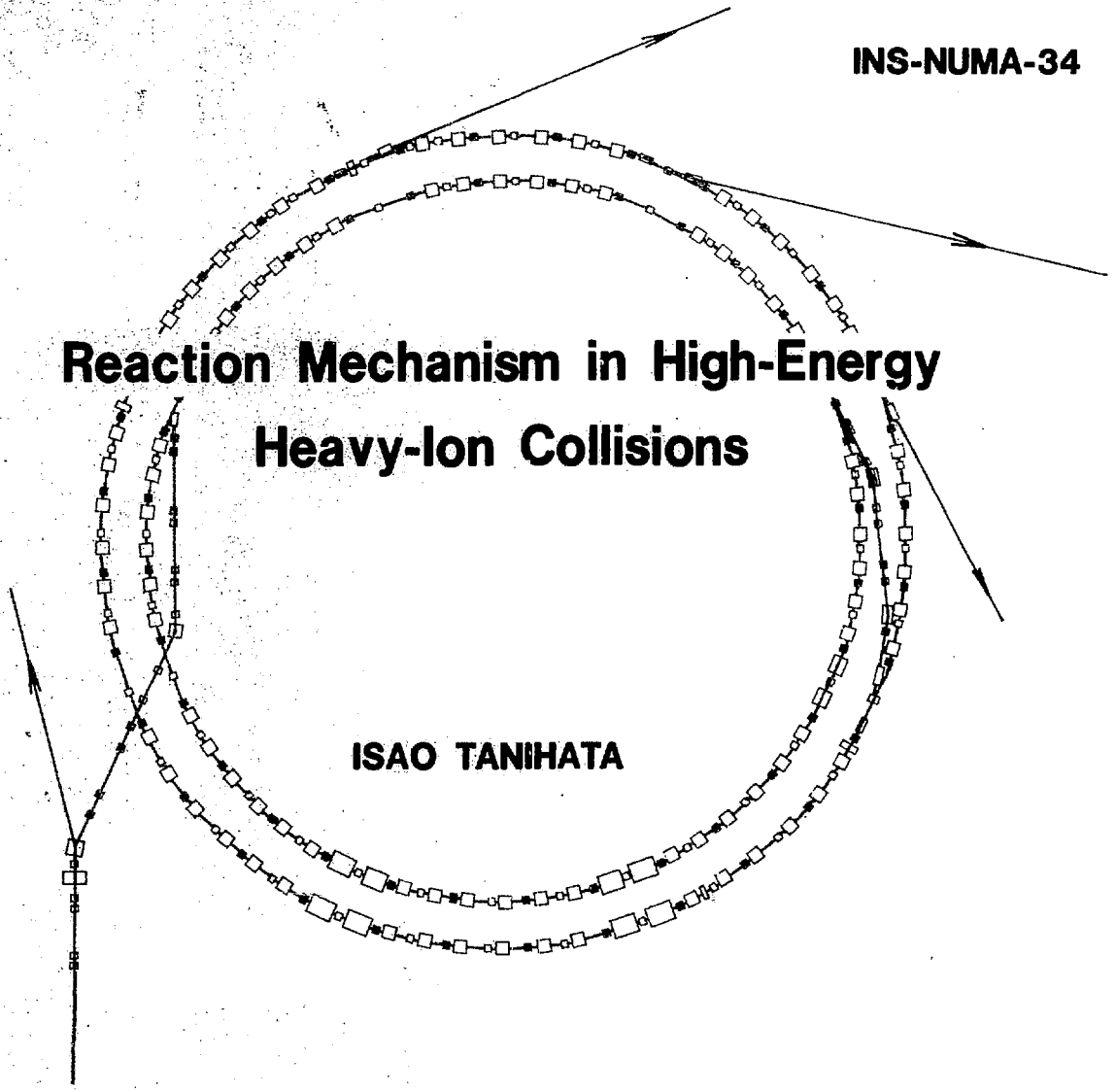

Reaction Mechanism in High-Energy Heavy-Ion Collisions

ISAO TANIHATA

April, 1982

STUDY GROUP OF NUMATRON AND
HIGH-ENERGY HEAVY-ION PHYSICS
INSTITUTE FOR NUCLEAR STUDY
UNIVERSITY OF TOKYO
Midori-Cho 3-2-1, Tanashi-Shi,
Tokyo 188, Japan

INS-NUMA-34
April 1982

Reaction Mechanism in High-Energy Heavy-Ion Collisions

ISAO TANIHATA

Institute for Nuclear Study, University of Tokyo
Tanashi, Tokyo 188, JAPAN

Presented at Nichidai Seminar in Karuizawa, October 23-25, 1981, also at the meeting for Heavy Ion Study at RCNP Osaka University, December 3-5, 1981.

I. Introduction

Since beams have become available at several accelerators, a variety of experimental data of high-energy(HE) heavy-ions(HI) have been accumlated. At the early stage of this field, production of new phases of nuclear matter was speculated on theoretically.[1] Most of these speculations were based on an expectation that a high-density would be achieved in the early stage of the HE-HI collisions. Several experiments have been performed with the hope of detecting a signal of such new phenomena. Instead of finding exciting phenomena, it was found that search for them was not as easy as had been expected.

While struggling to find the new phenomena, experimentalists found that the collision processes even under normal conditions were not well understood yet. Instead, they found that it is very important and interesting to investigate the reaction mechanism itself. In the earliest period, measurements of projectile fragmentation,[2,3] were performed which gave us the participant-spectator picture of the collision. Fig. 1 shows the rough idea of the last stage of a HI collision. In the coordinate space, the fragments (Fig.1-a), which are the group of nucleons that did not suffer hard collisions, are moving at the same velocity as the incident nucleons. Participants, which are the group of nucleons which mutually interacted, come from the interaction region which might have been in a state of high density and high temperature in an earlier stage of the reaction. In momentum space,(Fig.1-b), which is the space observed in the experiment, the fragments are

seen as two peaks at the momentum of the initial nucleons. The participants are distributed in a wide range of momentum showing a broad peak at zero momentum in the center of mass.

Measurements of the participants were at first the single particle (π,p,d....) inclusive cross sections.[4,5] The general features of the inclusive cross sections will be discussed in chapter four. A variety of models under different dynamical assumptions gave reasonable fits to the data. They ranged from the complete thermalization of the participant system to the single hard scattering of nucleons. On the other hand, the mean free path of nucleons inside the normal nucleus[6] is the same order of magnitude as the size of reaction region.[7-9] Thus it is hard to believe that either of these extreme assumptions in the theories are valid. To understand the dynamics of the reaction especially in the fast stage of the collisions, a more detailed analysis of inclusive cross sections including mass dependence, and beam energy dependence were made. Also, a new generation of experiments including measurements of two-particle correlations and of semi-inclusive cross section have been made. They showed that the reaction mechanism consisted of a mixture of several different mechanisms rather than any single one.

In this talk I would like to summarize our understanding of HE-HI collisions based on <u>experimental</u> data. My aim is mainly to show what has been learned and what are the problems we have to solve experimentally. Thus, theoretical models will be cited soley for understanding the experimental data. In the following two chapters (Ch. II, III) the geometrical aspects of the collisions will be discussed in relation to the total and the

reaction cross sections and to the average multiplicities. General features of the inclusive cross sections will be discussed in chapters IV and V. Several experimental data which have a close relation to the dynamics of the heavy-ion collisions will be discussed in chapter VI. I will not try to cover all the available data in this field. Of cource there are plenty of interesting experiments not discussed in this talk. I hope readers refer to the refereces in this paper as well as the summary papers[10] which appeared elsewhere. My main aim here is to show the overall idea of high energy heavy ion collisions and to give a few interesting (at least for me) directions for the future.

II. The Total and the Reaction Cross Sections

The total cross sections, σ_t, of nucleus-nucleus reactions as well as the reaction cross sections, σ_R, have been measured by Jaros et al. for many target-projectile combinations at 0.87 GeV/A and 2.1 GeV/A.[11]. The cross sections are well described by the equations,

$$\sigma_t = 144\ (A_T^{1/3}+A_P^{1/3}-1.48)^2\ \text{mb},$$

$$\text{and } \sigma_R = 78\ (A_T^{1/3}+A_P^{1/3}-1.25)^2\ \text{mb}.$$

The reaction cross sections have also been measured with heavier projectiles (α, ^{12}C, ^{14}N ^{16}O and ^{40}Ar) at energies of 2.1 GeV/A[12,13] and 0.5-0.2 GeV/A.[14] A parametrization of reaction cross sections of the form

$$\sigma_R = \pi r_o^2\ (A_T^{1/3}+A_P^{1/3}-\Delta)^2, \qquad (1)$$

where r_o = 1.29 fm, was found to be correct to within 10% for all beam and target combinations.[15] Also, σ_R is found to be independent of beam energy down to 0.15 GeV/A.[14] Thus the total and the reaction cross sections are quite consistent with the geometrical cross sections with diffused surface reflected by Δ in the equation.

The total cross sections are also understood reasonably well by microscopic calculations. Fig.2 shows a calculation based on Glauber theory for collisions of identical nuclei.[11] As can be seen, the fit to the data is satisfactory. Another type of microscopic calculation based on nucleon-nucleon cross sections has been made for p + Nucleus and n + Nucleus reactions by DiGiacomo et al.[16] When they take the effects of the real nuclear potential, the Coulomb potential, Pauli blocking, and Fermi motion into account, the calculations reproduce the experimental data σ_R for projectile energies from 15 MeV through 1 GeV. Their calculations as well as the experimental data are shown in Fig. 3. The calculations also reproduce the energy independence of the cross sections from 100 MeV to 1 GeV. It is interesting to see whether this approach can reproduce the experimental data on nucleus-nucleus collisions as well.

In summary, the nucleus-nucleus total and reaction cross sections are well described by the geometrical size of the colliding nuclei. The cross sections are also understood by microscopic calculations. This is basically a reflection of the fact that nuclei are thick enough for incident nucleons to make at least one scattering with nucleons inside the target over most of the overlapping region.

The excitation functions of the cross sections have not been measured in fine steps of projectile energy. It is very interesting to search for an anormaly in the total and the reaction cross sections in the future.

III. Average Multiplicities

The charged particle multiplicity gives additional information about the geometrical aspect of HI collisions. In the geometrical (participant-spectator) model the average number of participant protons (N_p) are calculated as

$$N_p = (Z_p A_T^{2/3} + Z_T A_p^{2/3}) / (A_p^{1/3} + A_T^{1/3})^2 \qquad (2)$$

where Z_p (Z_T) and A_p (A_T) are the atomic and the mass number of the projectile (target), respectively. Experimentaly the charged particle multiplicity, or the number of charged participants, was obtained from the integration of the inclusive cross sections of charged particles.

In Fig. 4 the comparison of the experimental data to Eq.2 is shown. Good agreement between the participant-spectator model and the data is seen over a wide range of projectile and target combinations. Therefore, it indicates that the number of nucleons involved in the collisions is mainly determined by the geometry of the collision.

Slight deviations from the geometrical estimations are seen in the energy dependence. The observed multiplicities of asymmetric combinations (Ne+Cu and Ne+Pb) are larger for higher incident energy. An interesting analysis was done in this regard by Gutbrod et al.[17]. They showed (see Fig.5) that

the average associated multiplicity scaled with the kinetic energy of the projectile for all types of projectiles. Where 'associated' means that the multiplicity measured when a proton (deuteron or trisium) with energy between 40 and 200 MeV was detected at 90^{o} in the laboratory. In Fig. 6, our data are plotted against the total kinetic energy of the projectile for a lead target. Our data are also consistent with a scaling with total projectile kinetic energy.

These data suggest that the total energy, independent of projectile size, is of most importance in determining the multiplicity. This energy dependence is puzzling because we know that the geometrical model is reasonably good for explaining several different feature such as the total and the reaction cross sections and the projectile fragmentation (see following chapter) in this energy region. Unfortunately we have no good answer for this problem now.

The energy dependence of the multiplicity is related to the nuclear stopping power and the transverse communication during the collision processes. It is thus very interesting as a future experiment to measure the energy dependence of the multiplicity in a systematic way.

IV. Overlook of Inclusive Spectra

Fig. 7 shows a sketch of the inclusive proton spectrum in a heavy ion collision. Two distinct regions can be seen in the spectrum. One is the fragment region seen as sharp peaks near the projectile and target rapidities (see Fig. 7-c). Particles emitted without violent N-N collisions are concentrated in this region. The other is the participantregion. Participant

nucleons which undergo at least one violent collision are distributed over a wide kinematical range.The exponential behavior of the spectrum (see Fig. 7-b) is a typical feature. The cross section is not isotropic but shows forward and backward peaking.

Fig. 8 shows an inclusive pion spectrum. Because pions must be produced in the collision no fragmentation peak is expected. At large P_T the pion spectrum also shows an exponential behavior as protons. In the low P_T region the pion spectrum differs from that of protons. One is a peak(dip) seen in the π^- (π^+) spectrum at beam rapidity and the other is a 90° enhancement of the π^+ spectrum. These spectral shapes are reasonably well explained by the Coulomb interactions of pions with nuclear fragments. Fig. 9 shows a model calculation of the Coulomb effect for π^+ and π^- [18]. A peak (dip) of the π^- (π^+) spectrum at beam rapidity is reproduced very well by the calculations. Actual fitting to the data is shown in Fig. 8-b.

The enhancement of the π^+ spectrum at 90° is also qualitatively reproduced by the same calculation. However, other possible mechanisms for the 90° enhancement such as hydrodynamical flow or Δ-Δ contributions[19] are not excluded. A most crucial point is the measurement of the π^- spectrum in this region because π^- will be enhanced by these effect in contrast to the Coulomb effect by which π^- is suppressed. Unfortunately no systematic measurements has been reported so far.

Now we take a little more detailed look at each region of the reactions.

V. Fragmentation Region

The process of fragmentation is generally separated into two stages. One is the abrasion stage, in which the incident nucleus reacts with the target nucleus and produces spectators and the participant. The other is the ablation stage in which the slightly excited nuclear fragments de-excite by emitting several particles. The ablation stage can be treated by the method of conventional low energy nuclear physics.

Fig.10-a shows the longitudinal momentum ($P_{//}$) dependence of ^{10}B fragment from ^{12}C at 2.1 GeV/A in the projectile rest frame [20]. The spectrum is well described by a Gaussian with an rms width, $\sigma(P_{//})$, and mean value ($P_{//}$). The rms widths, $\sigma(P_{//})$ and $\sigma(P_T)$, are equal within 10%. The general trend of $\sigma(P_{//})$ for different fragments is reproduced by the expression $\sigma(P) = 2\sigma_o \left\{ \frac{A_F}{A_p}(1-\frac{A_F}{A_p}) \right\}^{1/2}$ where A_F and A_p are the masses of the fragment and the projectile, respectively. The dependence of $\sigma(P_{//})$ on fragment mass is explained by several models[20-23].

Fig.8-c shows the production cross sections for different mass nuclei,[24] a strong dip at mass number eight shows the importance of the ablation stage of the reaction. On the other hand the sum of the masses of the projectile fragments should be independent of ablation and depend only on the abrasion mechanism. Such a measurement was reported recently by Stevenson et al.[25] Fig.8-b shows the summed mass distributions of the projectile fragments in ^{20}Ne+C and ^{20}Ne + Mo reactions. The two Spectra show big differences at

small mass ($A \leq 10$). This trend can be understood reasonably well by the effect of the size difference. In the ^{20}Ne + C case, the projectle, (^{20}Ne), is larger than the target, (^{12}C). Therefore there will always be a non-overlaping part in the projectile for all impact parameters. Thus fragments with very small mass are not expected. On the other hand in the Ne + Mo case, the projectle is smaller than the target nucleus. No fragment is expected when the impact parameter is smaller than a certain value and thus small mass fragments are enhanced. Curves in the figure show the model calculation of abrasion in which the portion of the projectle nucleus that misses the target sphere forms the projectile residue. The success of the model indicates the validity of the geometrical aspect of the collision in the fragmentation processes.

Combining these results with the information on total cross section and the total reaction cross section we can conclude that the HE-HI reaction occurs in the overlap region of the projectle and target. This conclusion has been tested by measuring the number of participants for various reactions as discussed in chapter III.

Because nuclei have diffused surfaces, a collision with an impact parameter approximately equal to the nuclear radius should show some trasparency. However a detailed study of this subject has not been done yet.

Before finishing this chapter, I would like to show a good application of fragmentation in investigating the internal momentum distribution of nucleons. Fig. 11 shows the P_T and P distributions of ^3He and ^3H fragments in ^4He + C reactions. Theoretical calculations including the three

processes shown in Fig. 11-a were done by Fujita and Hüfner.[26] They found that the $P_{//}$ distribution is mainly governed by the SP process(Fig. 11-c). This means that the momentum distribution of ^{3}He(or ^{3}H) inside ^{4}He is directly reflected in the $P_{//}$ spectrum. In other words the $P_{//}$ spectrum gives direct information on the momentum distribution of ^{3}He(or p in turn) inside ^{4}He. The deviation of the calculated curve (solid line in Fig. 11-c) suggests the existence of a long non-Gaussian momentum tail.

VI. Space and Time Structure of the Collisons

So far we have discussed mainly the geometrical aspect of the HE HI reactions and fragmentations. From now on our discussion will be restricted to the physics of the participant. First, the space and the time structure of the collisions will be discussed in this chapter. The dynamical aspects of the collisions will be discussed in the following chapter.

It is very interesting to know how reactions develop and how particle emission occurs. Unfortunately we have no experimental method to follow the time sequence of the reaction. However, several methods to determine the average time of the reaction and the freeze-out volume can be applied. The freeze-out volume is defined as the volume of the participant region when the participant nucleons no longer interact significantly with each other. Three methods will be discussed. They are measurements of

i) the cross section of composite particles,

ii) the two-proton correlation function at small relative momentum, and

iii) the two-pion correlation function at small relative momentum.

Let us start the discussion from the inclusive cross section of composite particles. An interesting relation was found between the composite particle spectrum and the proton spectrum. The two spectra are related by

$$E_A \frac{d^3\sigma_A(\vec{P}_A)}{d\vec{P}_A} = C \left(E_p \frac{d^3\sigma_p}{d\vec{P}_p}\right)^A ,$$

$$\vec{P}_A = A\vec{P}_p$$

where C is a constant which may differ for different combinations of projectile and target. An example is shown in Fig.12-a, in which the deuteron inclusive spectra (solid circles) are plotted along with the square of the proton spectra (open circles). In the frame work of the thermal model the constant C is related to the freeze-out radius.[7,27] Here I show only the results of analysis. The constant C was found to be independent of beam energy between 400 MeV/A and 2.1 GeV/A. The obtained radii, R, are tabulated in Table I.

Basically the deuteron spectra result from the final state interaction between a proton and a neutron. The final state interactions between two protons also affect the spectra. In this case, correlations appear only between protons of small relative momentum since no bound state of two protons exists. Three types of interactions are involved between protons. They are Coulomb interactions, strong interactions and exchange interactions due to the fermion nature of the proton.

The correlation function (R) is defined as

$$R(|P_1 - P_2|) = \left[\frac{d^6\sigma}{d\vec{P}_1 d\vec{P}_2} \Big/ \frac{1}{\sigma_R} \frac{\langle n(n-1)\rangle}{\langle n\rangle^2} \frac{d^3\sigma}{d\vec{P}_1} \frac{d^3\sigma}{d\vec{P}_2} \right] - 1 \quad \cdots(3)$$

The experimental data are shown in Fig.12-b along with calculated curves using a Gaussian shape source with rms radii r_o=2,3 and 4 fm[9].

An interesting fact observed here is that the apparent sizes are different depending on the kinematics of the observed protons. The reaction size looks larger when protons are observed near beam rapidity (Y_B) (P_T=0.2-0.4 GeV/c) than the when they are observed at intermediate rapidity ($Y_{B/2}$). This tendency can qualitatively be understood because protons from the projectile fragments as well as the participant protons are included near beam rapidity. In the region of intermediate rapidity, on the other hand, only participant protons contribute. Thus the apparent reaction volume can be larger at the beam rapidity.

The third method is interferometry based on the Hanbury Brown-Twiss effect of two like pions. The enhancement of events with two like-pions small relative momentum is expected. The correlation function of eq.(3) gives the mean separation of pions in space and time. Fig.12-c shows the observed correlation in two axes namely the time and the space axes which are conjugate to the energy and the momentum of the measured pions, respectively.[28,29] Curves in the Figure are the theoretical fit to the data with R=1.7 fm and ct=3.21 fm.[30,31]

Table 1 summarizes the interaction radii and the reaction times obtained by these three methods. The obtained size of the reaction region ranges from 2 to 4 fm and to lowest order agrees with the size of the overlapping region of two colliding nuclei . However the meaning of the term 'size' used here is not perfectly clear.

To determine the reaction radius, we need at least two important assumptions. One is the distribution function of the source itself. Depending on the choice of the spacial shape of the emitting source, for example Gaussion or, exponential or even anisotropic, the determined radius varies on the order of 1 fm.

Also because the reaction size is generally different for different impact parameters further complications arise through the need to treat the average size. In the two-proton correlation experiment, the apparent size depends on where the two protons are detected (Y_B or $Y_{B/2}$). However no such diference was observed in the analysis of deuteron production. A slight difference in the observation angles between the proton and deuteron experiments may be one of the reason. But this is not yet clear. Hence it is necessary to clearify the situation.

Another point is that the final state interaction itself also introduces problems. Corrections for the Coulomb interactions between two particles are not difficult but the Coulomb interactions between the observed particles and the remaining system constitute essentially a many body problem which is difficult to solve.

Moreover, especially in deuteron production, the mechanism of production is not well known. Several models such as thermal, sudden approximation, and time-dependent perturbation gives different relationships between the obseved spectrum and the reaction radius.[32] Thus we need a further theoretical study to get more detailed information on the reaction size.

On the experimental side the data is mostly impact-parameter averaged. The separation of data for different impact parameters will certainly simplify the problems. Measurements have been reported with an impact parameter bias for both 2p and $2\pi^-$ correlations. For high-multiplicity events(small impact parameter), the 2p experiment[29] showed a smaller volume than the impact parameter averaged data while the 2π experiment reported a larger volume.[29] At this moment we have no idea what is the main source of this discrepancy. Further detailed experimental as well as theoretical studies are desirable.

VI. Dynamics of the Collision

i) Inclusive Spectra

So far I have shown data mainly related to the bulk properties of the collisions:the total reaction cross sections, the average multiplicities, the fragmentations of the nuclei, and the space and the time structure of the reactions. We have learned that the geometrical aspect of the collision, the participant spectator separation, was found to be reasonable as

a basic concept. We now look at the spectra in more detail to obtain an insight into the dynamics of the collisions.

The single particle inclusive cross sections of π,n,p,d,t.... were measured by several groups[4-9,33-34]. Many theoretical models: the hard scattering models[35,36], linear cascade models,[37,38] three dimensional cascade[39,40], the transport theoretical models,[41] the classical equation of motion[42,43], the statistical models,[44,45] the collective tube models,[41,42] thermal models,[27,48] hydrodynamical models,[49-52] were proposed. Most of them explain the inclusive cross sections reasonably well.

It is obvious that some of the basic dynamical assumptions of these models mutually contradict. Then, why can these models explain the experimental data? Our understanding now is that the agreement is due to the geometrical aspect of the models rather than their dynamical assumptions. Integration of the inclusive cross section over the momentum gives,

$$\int E\frac{d^3\sigma}{d\vec{P}}\cdot\frac{d\vec{P}}{E} = \langle m\rangle\,\sigma_R$$

where σ_R is the reaction cross section and $\langle m\rangle$ the average multiplicity of the particle. As already discussed in the previous chapters, the reaction cross sections as well as the average multiplicity are mainly determined by the geometry of the collision. Thus any models with the participant-spectator picture of the reaction built in gives a resonable size for the cross section. The shapes of both momentum and angular distributions should also be fit by the models. However each model has its own set of parameters to describe these

distributions. The temperature(or freeze-out density) is the one for thermal models and the effective Fermi momentum distribution is the one for the hard scattering model. Therefore the agreement to the data is not really a test of the models of which I believe the dynamical concept is meaningful to separate one to the other. The fitting of the inclusive cross sections to a factor of two or so does not prove more than the validity of the geometrical concept.

To investigate the dynamics of the collisions we have to either rely on the details of the spectra such as mass dependences, angular distributions, and energy dependences or perform different kinds of measurements such as semi-inclusive cross sections and particle correlations. In the sections below we will investigate these items one by one and try to learn what they are telling us.

a) Angular Distributions

The angular distributions of protons and pions in the c.m. frame are shown in Fig.13. Ratios of the cross sections at 30° in the c.m. and at 90° are plotted as a function of c.m. energy. For protons, strong forward and backward peaking is observed (the angular distribution is symmetric along 90° for collisions of same mass nuclei) specially at high energy. For pions, the anisotropy shows a maximum at around 150 MeV. At lower energy Chiba et al.[53,54] and Wolf et al.[55] found that the angular distribution is almost isotropic even showing a slight enhancement at 90°. Their data at energies around 150 MeV were consistent with our data showing forward-backward peaking. At a beam energy of 800 MeV/A a similar behavior was observed for C+C and Ne +NaF,[35] reactions.

These features can not be explained by any conventional theoretical model. For example the firestresk model[48] and the hard-scattering model[35] both predict too large anisotropies for high-energy protons. For high-energy pions the firestreak model predicts a too small anisotopy while the hard-scattering model predicts a too large one. Neither of the models explain the maximum of the anisotropy at 150 MeV in pions. Naively, 150 MeV corresponds to the energy of pions emitted from Δ decay. It is therefore very difficult to understand why the hard scattering model can not predict the maximum.

b) Mass Dependences of the Cross section

Let me show mass dependences of the inclusive cross sections in different kinematical regions. The mass dependence of the cross sections for collisions of identical nuclei are well described by the form $d\sigma/dpd\Omega \propto A^{\alpha}$, where A is the mass number of the projectile and target. The fitted values of α are plotted in Fig. 14 as a function of momentum. At a forward angle (15°) α is close to the geometrical value(5/3) excepted at very high momentum, thus indicating the importance of single scattering.

On the other hand α is much larger at large scattering angle, say at 90°, in the c.m.. The factor α is more than 2.5 at the highest energy, that is stronger than an $A_T A_P$ dependence, and no saturation is seen yet. This strong mass dependence suggests that multiple scattering or some collective behavior of nucleons is taking place. Pions show almost the

same behavior as shown in Fig. 12b at 90° in the c.m.. The reason why pion and proton have the same dependence on the c.m. kinetic energy is not understood. However the similarity is too strong to say it is a mere coincidence.

c) Slope Factor of Energy Spectra

Inclusive cross sections of light paricles show an exponential behavior at 90° in the N-N c.m. frame

$$\frac{1}{P}\frac{d\sigma}{dEd\Omega} \propto e^{-E/E_0}$$

The slope factor E_0 is plotted against the c.m. beam energy in Fig. 15. In general, E_0 inclease montonically with beam energy. The value of E_0 saturates at c.m. beam energies higher than 1 GeV. The limiting value of E_0 is about 140 MeV. The slope factor of the particle spectra in p-p collisions also shows a limiting behavior with similar values for E, 150 MeV.[56] Since the limiting value is so similar for the two cases the mechanism which produces the slope is probably the same.

Two curves in the figure show the predictions of two theoretical models. One is the hard scattering calculation which is a model of the extreme single nucleon-nucleon type. The slope factor is determined mainly by the momentum distribution of the nucleons in the projectile and the target. The effective momentum distribution was selected so as to fit the cross section at 800 MeV. By this calculation, the slope factor is limited at much lower energies than it is in the data.

The other curve shows the opposite extreme, namely the thermal model.[27] This model includes the freeze-out density, (ρ), as a parameter, as seen in the equation below.

$$E_B^*/A = \frac{3}{2}T + 2.28\frac{\rho_o}{\rho}\left(\frac{T}{m_\pi c^2}\right)^{9/2} m_\pi c^2$$

where E_B^*/A is the center of mass energy per nucleon, ρ_o and T are the normal nucleon density and temperature of the thermalized system, respectively. The temperature, which corresponds to the slope factor of the spectrum, can not uniquely be determined from this equation only. The model, however, also predicts the ratio of the number of pions to the number of nucleons(Z) as,

$$\pi^-/Z = 0.46(\rho/\rho_o)\ (T/m_\pi c^2).$$

From these two equations we can get a direct relation between π^-/Z and T independent of ρ/ρ_o. Curves in the figure are drawn using the experimental values for π^-/Z.[4] This curve shows saturation at a higher energy than the data. This thermal model doesn't include the baryon spectra. It is reasonable that the inclusion of heavier baryons makes the temperature lower and causes saturation at a lower energy.

In fact a calculation based on nuclear matter suggests that the energy dependence of the slope factor is determined by the baryon mass spectrum.[57] If multiple collision processes dominate in the high P_T region, this idea would be an interesting suggestion containing a possibility of detecting nuclear matter consisting of many baryons. However the theoretical calculations are not yet done at a level to compare with the data.

ii) Two Paricle Correlations

Measurements of two-particle correlations have been made between light particles[58] and between light and heavy particles.[17] Here I show two intresting examples which show different features of heavy ion collisions. In one experiment[58] a coplaner type correlation function $C(\theta,P)$,

$$C(\theta,P) = \frac{2\cdot(S(\theta,P)\cdot R)/R}{(S(\theta,P)\cdot U)/U + (S(\theta,P)\cdot D)/D}$$

are measured. Where $(S(\theta,P)\cdot R)$ ($S(\theta,P)\cdot U$ or $(S(\theta,P)\cdot D)$) indicates the coincidence rate between a spectrometer located at $\varphi=0$ and a R(U or D) coincidence telescope, which is located at $\theta=40^{\circ}$ and $\varphi=180^{\circ}$ (90° or -90°). The symbol R(U or D) is the single counting rate of the telescope. Particles with longer range than a proton of energy greater than 200 MeV are detected in the telescopes. Figs.16,17 show the observed correlation function in the nucleon-nucleon center of mass frame. The momentum per nucleon of the projectile and target are indicated by solid circles. Dotted circle shows the kinematic loci for elastic scattering of two nucleons. In the collisions of light ions C+C or Ar+Ar (see Fig.16) the correlation function shows a clear peak just oposite to the kinematical region of the R-counter (shown by the shadowed area). This gives clear evidence for the existence of Quasi-Elastic-Scattering(QES) of nucleons in these HI collisions. A simple analysis of the data shows about a 20% contribution of the QES process in this kinematical region.[58]

In contrast to the case of light ions, a completely different type of correlation was observed in the case of heavier targets (C+Pb, Ar+Pb) as shown in Fig.17. An important feature is that the correlation pattern is stronger in heavier projectile and target combinations. This contrasts with the QES case in which the correlation was smaller for heavier target and projectile combinations . Thus, Fig.17 suggests that this correlation is related to the many body nature or the collectiveness of the nucleus.

Here I show an interesting theoretical calculation by Stocker et al. based on a hydrodynamical model.[59,60] As shown in Fig.18, their calculations give a so called bounce off effect of the projectile by the target nucleus. According to the model the coincidence counters effectively select an impact parameter of about 6 fm which corresponds to Fig. 18-b. The target nucleus recoils in the opposite direction of the bounced projectile and thus gives a large cross section at a large angle on the side opposite to the coincidence counter. On the other hand, less particles are emitted at small angles.

Experimental data and the result of the model calculations of the correlation function are compared in Fig. 19. Although there is quantitative disagreement, they show good agreement in the overall shape of the correlation function. If this theoretical model is the appropriate one for these nuclear collisions, the possibility of searching for highly-compressed matter is almost at hand. We need further experimental data including a dependence on the angles of the coincidence counter and a dependence on impact parameter.

Cascade calculations are also in progress[61] and we would find the validity of hydrodynamics in these projectile and target combinations.

Similar correlations have been observed in heavy fragment and light particle coincidence data[17]. Fig.20 shows that, when a heavy fragment is detected at 90° in the laboratory, more light particles are emitted into the forward direction of the opposite side. These correlations are also consistent with the hydrodynamical calculations and complementary to the light-particle correlations.

VIII. Closing

In this talk I have tried to show the experimental data obtained in high-energy heavy-ion collisions. My main effort was to show what we have learned from the experimental data with minimum theoretical bias. I didn't cover all the available experimental data uniformly in any sense. However I hope this talk gives you an overall idea of high-energy heavy-ion collisions. Persons who have interest in more detail are recommended to read the references. A particularly good start would be Ref. 10 which is an excellent source of the information on this and related subjects. Thank you.

References

1. For references of these subjects see Proceedings of 2nd High Energy Heavy Ion Summber Study, Lawrence Berkeley Laboratory Report LBL-3675, and references there in.
2. D.E. Greiner, P. J. Lindstrom, H. H. Heckman, B. Cork, and F. S. Bieser, Phys. Rev. Letters 35(1974) 152.
3. A. S. Goldhaber and H. H. Heckman, Ann. Rev. Nucl. Sci. 28(1979) 161.
4. Experimantal data as well as the comparison to theoretical models are seen in, S. Nagamiya, M.-C. Lemaire, E. Moeller, S. Schnetzer, G. Shapiro, H. Steiner, and I. Tanihata, Phys. Rev. C 24(1981) 971.
5. J. Gosset, H. H. Gutbrod, W. G. Meyer, A. M. Poskanzer, A. Sandval, R. Stock, and G. D. Westfall, Phys. Rev. C 16(1977) 629
6. I. Tanihata, S. Nagamiya, S. Schnetzer and H. Steiner, Phys. Letters, 100B(1981) 121
7. M.-C. Lemaire, S. Nagamiya, S. Schnetzer, H. Steiner and I. Tanihata, Phys. Letters, 85B(1979) 38
8. S. Y. Fung, W. Gorn, G. P. Kiernan, J. J. Lu, Y. T. Oh and R. T. Poe, Phys, Rev. Lett. 41(1978) 1592.
9. F. Zarbakhsh, A. L. Sagle, F. Brochard, T. A. Mulera, V. Perez-Mendez, R. Talaga, I. Tanihata, J. B. Carroll, K. S. Ganezer, G. Igo, J. Oostens, D. Woodard, and R. Sutter, Phys. Rev. Lett. 46 (1981) 1268.

10. Excellent reviews are seen in the proceedings of Hakone Seminar on "High-Energy Nuclear Interactions and Properties of Dense Nuclear Matter" (k. Nakai and A. S. Goldhaber, ed.)

11. J. Jaros, A. Wagner, L. Andersom. O. Chamberlain, R. Z. Fuzesy, J. Gallup, W. Gorn, L. Schroeder, S. Shannon, G. Shapiro, and H. Steiner, Phys. Rev. C 18(1978) 2273.

12. H. H. Heckman, D. E. Greiner, P. J. Lindstrom, and H. Shwe, Phys. Rev. C 17(1978) 1735.

13. G. M. Chernov, K. G. Gulamov, U. G. Gulyamov, S. Z. Nasyrov, and L. N. Svechnikova, Nucl. Phys. A280(1977) 478.

14. R. Kullberg, K. Kristiansson, B. Lindkvist, and I. Otterlund, Nucl. Phys. A280(1977) 491.

15. P. J. Lindstrom, D. E. Greiner, H. H. Heckman, B. Cork, and F. S. Bieser, Proc. 14th Int. Conf. Cosmic Rays 1975 p2315.

16. N. J. DiGiacomo, R. M. DeVries, and J. C. Peng, Phys. Rev. Letters 45(1980) 527.

17. H. H. Gutbrod, "High-Energy Nuclear Interactions and Properties of Dense Nuclear Matter" Proceedings of the Hakone Seminar, at Hakone July 1980, ed. K. Nakai and A. S. Goldhaber, pp93.

18. S. E. Koonin, "High-Energy Nuclear Ineteractions and Properties of Dense Nuclear Matter" Proceedings of the Hakone Seminar July 1980, ed. K. Nakai and A. S. Goldhaber, pp326.

19. M. Sano, M. Wakai, and Y. Kitazoe, "High-Energy Nuclear Interactions and Properties of Dense Nuclear Matter" Proceedings of the Hakone Seminar at Hakone July 1980, ed. K. Nakai and A.G. Goldhaber pp302.

20. D. E. Greiner, P. J. Lindstrom, H. H. Heckman, Bruce Cork, and F. S. Bieser, Phys. Rev. Letters, 35(1975) 152.

21. H. Feshback and K. Huang, Phys. Letters 47B(1975) 152.

22. A. S. Goldhaber, Phys. Letters 53B(1974) 306.

23. J. Hüfner, K. Schafer, and B. Schurmann, Phys. Rev. C 12(1975) 1888.

24. P. J. Lindstrom, D. E. Greiner, H. H. Heckman, B. Cork and F. S. Bieser, LBL-report LBL-3650, 1975(unpublished).

25. H. I. Stevenson H. Nartubus, and P. B. Price, Phys. Rev. Letters 47(1981) 990.

26. T. Fujita and J. Hüfner, Nucl. Phys. A343(1989) 493.

27. A. Z. Mekjian, Phys. Rev. Letters 38(1977) 604, and Phys. Rev. C 17(1978) 1051.

28. J. A. Bistrlich et al. "High-Energy Nuclear Interactions and Properties of Dense Nuclear Matter" Proceedings of the Hakone seminar July 1980, ed. K. Nakai and A. S. Goldhaber, pp393.

29. S. Y. Fung, W. Gorn, G. P. Kiernan, J. J. Lu, Y. T. Oh, and R. T. Poe, Phys, Rev. Letters 41(1978) 1592.

30. S. E. Koonin, Phys. Letters 70B(1977) 43.

31. M. Gyulassy, S. K. Kauffmann, and L. W. Wilson, Phys. Rev. C 20(1979) 2267.

32. J. I. Kapusta, Phys. Rev. C 21(1980) 1301.

33. W. Schimmerling, J. Kast, D. Ortehdahl, R. Madey, R. A. Cecil, B. D. Anderson, and A. R. Baldwin, Phys. Rev. Letters 43(1979) 1985.

34. I. Tanihata, S. Nagamiya, O. Chamberlain, M.-C. Lemaire, S. Schnetzer, G. Shapiro, and H. Steiner, Phys. Letters 87B(1979) 349.

35. R. L. Hatch and S. E. Koonin, Phys. Letters 81B(1978) 1.

36. R. H. Landau and M. Gyulassy, Phys. Rev. C 19(1979) 149.

37. J. Hüfner and J. Knoll, Nucl. Phys. A290(1977) 460.

38. J. Knoll and J. Randrup, Nucl. Phys. A324(1979) 445.

39. Y. Yariv and Z. Fraenkel, Phys. Rev. C 20(1979) 2227.

40. J. Cugnon, Phys. Rev. C 22(1980) 1885.

41. H. J. Pirner and B. Schurmann, Nucl. Phys. A316(1979) 461.

42. A. R. Bodmer and C. N. Panos, Phys. Rev. C 22(1980) 1025, and Nucl. Phys. A356(1981) 517.

43. Y. Kitazoe, M. Sano, and K. Yamamoto, Nuovo Cimento Lett. 32(1981) 337.

44. J. Knoll, Phys. Rev. C 20(1979) 773.

45. S. Bohrman and J. Knoll, Nucl. Phys. A356(1981) 498.

46. J. Vary, Phys. Rev. Letters 40(1978) 294.

47. Meng Ta-Chung and E. Möller, Phys. Rev. Letters 41(1978) 1352.

48. J. Gosset, J. I. Kapusta, and G. D. Westfall, Phys. Rev. C 18(1978) 844.

49. A. A. Amsden, G. F. Bertsch, F. M. Harlow, and J. R. Nix, Phys. Rev. Letters 35(1975) 905.

50. Y. Kitazoe, K. Matsuoka, and M. Sano, Progr. Theor. Phys. 56(1976) 860.

51. L. P. Csernai and W. Greiner, Phys. Letters 99B(1981) 85.

52. J. R. Nix and D. Strottman, Phys. Rev. C 23(1981) 2548.

53. J. Chiba, K. Nakai, I. Tanihata, S. Nagamiya, H. Bowman, J. Ingersoll, and J. O. Rasmussen, Phys. Rev. C 20(1979) 1332.

54. K. Nakai, J. Chiba, I. Tanihata, M. Sasao, H. Bowman, S. Nagamiya, and J. O. Rasmussen, Phys. Rev. C 20(1979) 2210.

55. K. L. Wolf, H. H. Gutbrod, W. G. Meyer, A. M. Poskanzer, A. Sandoval, R. Stock, J. Gosset, C. H. King, G. King, Ngnyen Van Sem. and G. D. Westfall, Phys. Rev. Letters 42(1979) 1448.

56. B. Blobel et al., Nucl. Phys. B69(1974) 454.

57. S. I. A. Garpman, N. K. Glendenning, and Y. J. Karant, Nucl. Phys. A322(1979) 382.

58. I. Tanihata, M.-C. Lemaire, S. Nagamiya and S. Schnetzer, Phys. Letters. 97B(1980) 363.

59. L. P. Csernai, H. Stöcker, and W. Greiner, Univ. Frankfurt Report UFTP-36, 1981.

60. L. P. Csernai, W. Greiner, H. Stöcker, I. Tanihata, S. Nagamiya, and J. Knoll, to be published in Phys. Rev. C, LBL report No. 12660,1981.

61 M. Gylassy and K. Frankel, private communications.

62. K. Smith, Private communications.

63. L. Anderson, Thesis, Lawrence Berkeley Laboratory Report, LBL-6767(1977), unpublished.

Figure Captions

Figures with no citation are the data obtained by INS-LBL collaboration group. see refs. 1,4,6,7,9,25,33,35,54,58 for more details.

1. Final stage of heavy-ion collision in coordinate space (a) and in momentum space (b). The distribution in momentum space is cited from a cascade calculation by K. Smith.[62]
2. The total cross sections of heavy-ion collisions. Predictions by Glauber theory reproduce the data well. The figure is cited from ref. 11.
3. The reaction cross sections of proton-nucleus and neutron-nucleus reactions. Curves drawn in the figures are the results of the microscopic calculations based on nucleon-nucleon scattering cross sections. The figure is quoted from ref. 16.
4. Average multiplicities of charged particles are plotted against the average number of participant protons. Dotted line shows a prediction of a simple geometrical model.
5. Average associated multiplicities are shown as a function of total kinetic energy of the incident particle. Curves in the figure are only for guiding the eye. The figure is quoted from ref. 17.
6. Average multiplicity as a function of total kinetic energy of projectile. Curve is only for guiding the eye.
7. A sketch of the inclusive proton spectrum in heavy-ion collisions. Fig. c is quoted from ref. 63.

8. An inclusive spectrum of pions produced in heavy-ion collisions. Curves in (b) are the theoretical fit to the data. See text for detail. Fig. (b) is cited from ref. 18.

9. Model calculations of the Coulomb effect for π^+ and π^- production.[18] Contour lines are shown for no Coulomb interactions (b), π^+(a), and π^-(c).

10. (a) Longitudinal momentum, $P_{//}$, distribution of ^{10}B fragment from ^{12}C projectile at 2.1 GeV/A. The figure is quoted from ref. 19.

    (b) Summed mass distributions of the projectile in ^{20}Ne reactions. Curves in the figure are the results of the Fire-streak model. The figure is quoted from ref. 25.

    (c) Production cross sections of different mass nuclei. The figure is quoted from ref. 25. Data are from ref. 24.

11. P_T (b) and $P_{//}$ (c) distributions of ^3He and ^3H fragments. Classifications of production mechanisms are shown in (a). Figures are quoted from ref. 26.

12. (a) A comparison of deuteron spectra and the square of proton spectra.

    (b) The correlation function in two-proton coincidence spectra. Curves in the figure show the results of model calculations. Numbers beside the curves indecate the size of the reaction region.

    (c) The correlation function in two-pion coincidence spectra. Curves are the best fit to the data. The figures are quoted from ref. 28.

13. Ratios of the inclusive cross sections at 30° and 90° in the c.m. frame are plotted against the particle energy. Curves in the figure are only for guiding the eye.
14. The exponent of mass dependence, α, is plotted as a function of particle momentum.
15. The slope factors of the proton (•) and pion (o) spectra at 90° in the c.m. frame are plotted against the c.m. beam energy. The solid curve shows a prediction by the hard-scattering model and the broken line shows a result of the thermal model.
16. The coplanar correlation function in collisions of identical nuclei. Contour lines of the correlation function are drawn in the nucleon-nucleon c.m. system. Dashed lines in the figure indicate the loci of the elastic scattering. Shadowed areas indicates the kinematical region covered by the coincidence telescope R.
17. The coplanar correlation function in the the case of heavy targets.
18. Three dimensional differential cross sections calculated by a hydrodynamical model. Figures are quoted from ref. 59. Calculated cross sections are drawn for different impact parameters.
19. A comparison of the experimental data and a hydrodynamical and linear cascade calculations of the correlation function. The figures are quoted from ref. 60.

20. The correlation function of heavy fragment and light particle coincidence events. Zero in the correlation function indicates no correlation between two particles. Definition of the correlation function is the same one as written in Eq. 3 in the text. The figures are quoted from ref. 17.

Table 1

The reaction size and the reaction time obtained by i) deuteron production, ii) 2p-correlation, and iii) 2π-correlation measurements.

Method	Reference	Reaction	Beam Energy (Gev/A)	R (fm)	ct (fm)
i	4,7	Ne + NaF	0.4,0.8,2.1	3.4 +0.3	-
		Ar + Kcl	0.8	3.5 +0.4	-
		Ar + Pb	0.8	4.3 +0.4	-
ii	26	Ar + Kcl	1.8	2.2 (Y_B)	-
				1.75($Y_{B/2}$)	-
iii	28	Ar +Pb_3O_4	1.8	3.3 +0.9	1.5
	27	Ar +Kcl	1.8	1.8 +0.5	2.7+.7

Fig. 1

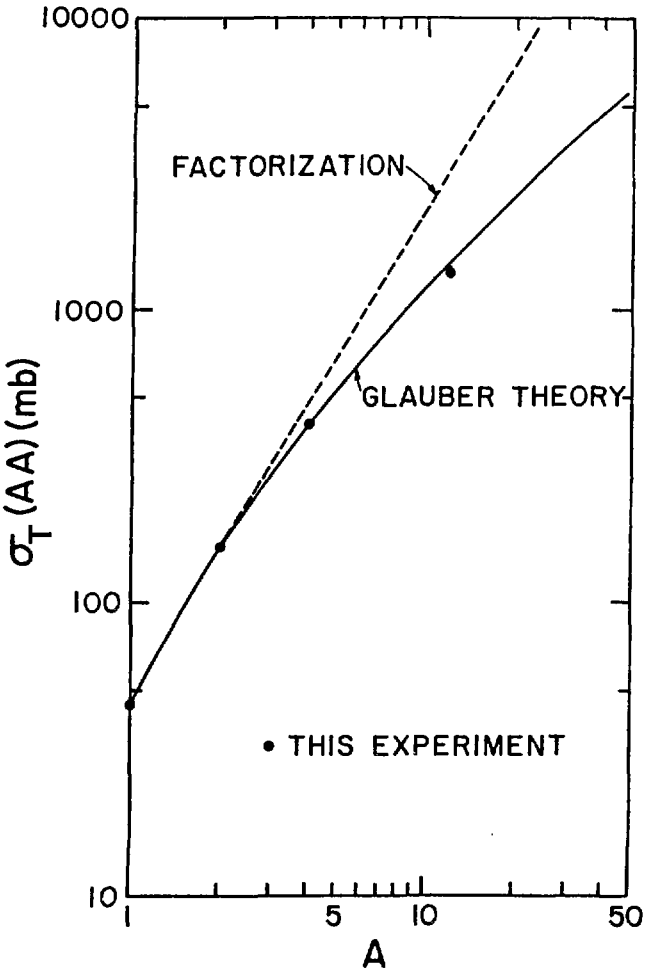

XBL 7511-9045

Fig. 2

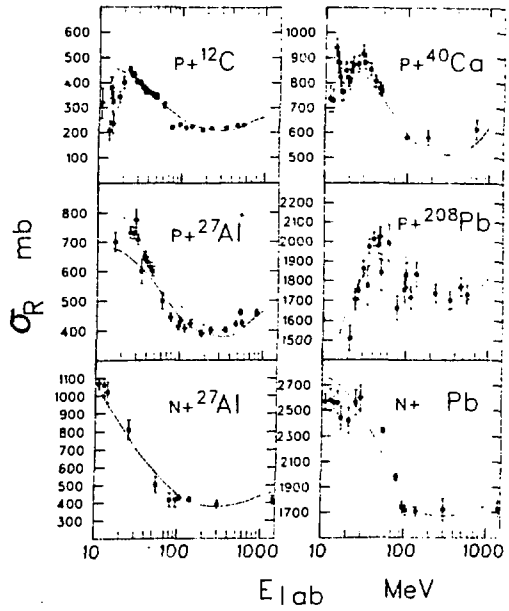

Fig. 3

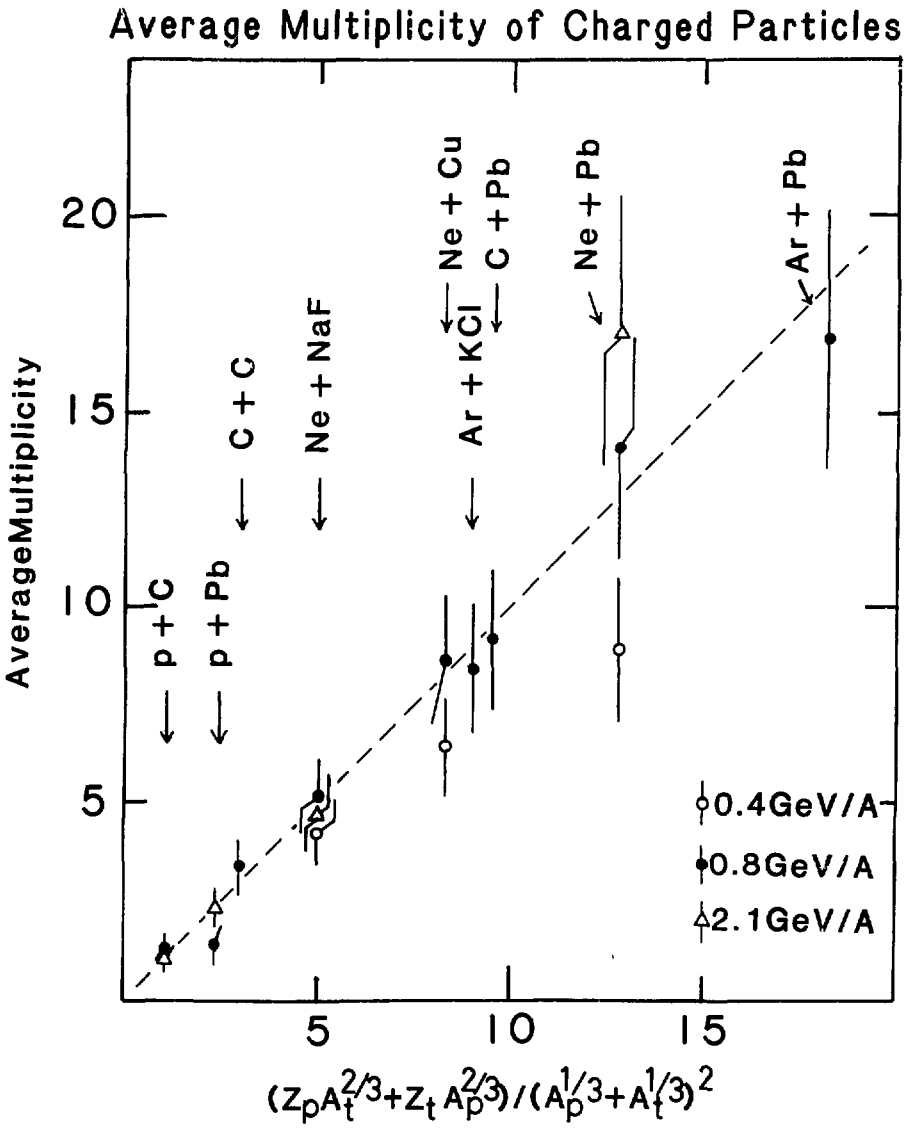
Average Multiplicity of Charged Particles
AverageMultiplicity
20
15
10
5
p + C
p + Pb
C + C
Ne + NaF
Ar + KCl
C + Pb
Ne + Cu
Ne + Pb
Ar + Pb
0.4GeV/A
0.8GeV/A
2.1GeV/A
5
10
15
$(Z_p A_t^{2/3} + Z_t A_p^{2/3}) / (A_p^{1/3} + A_t^{1/3})^2$

Fig. 4

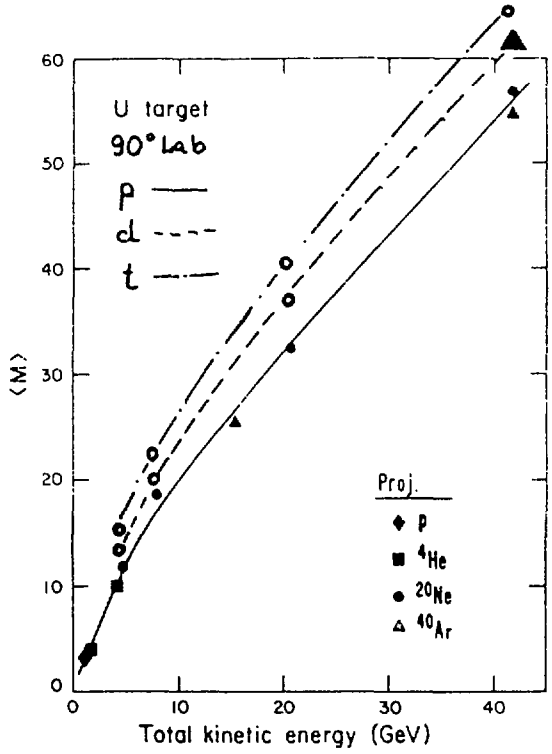

XBL 797-2054

Fig. 5

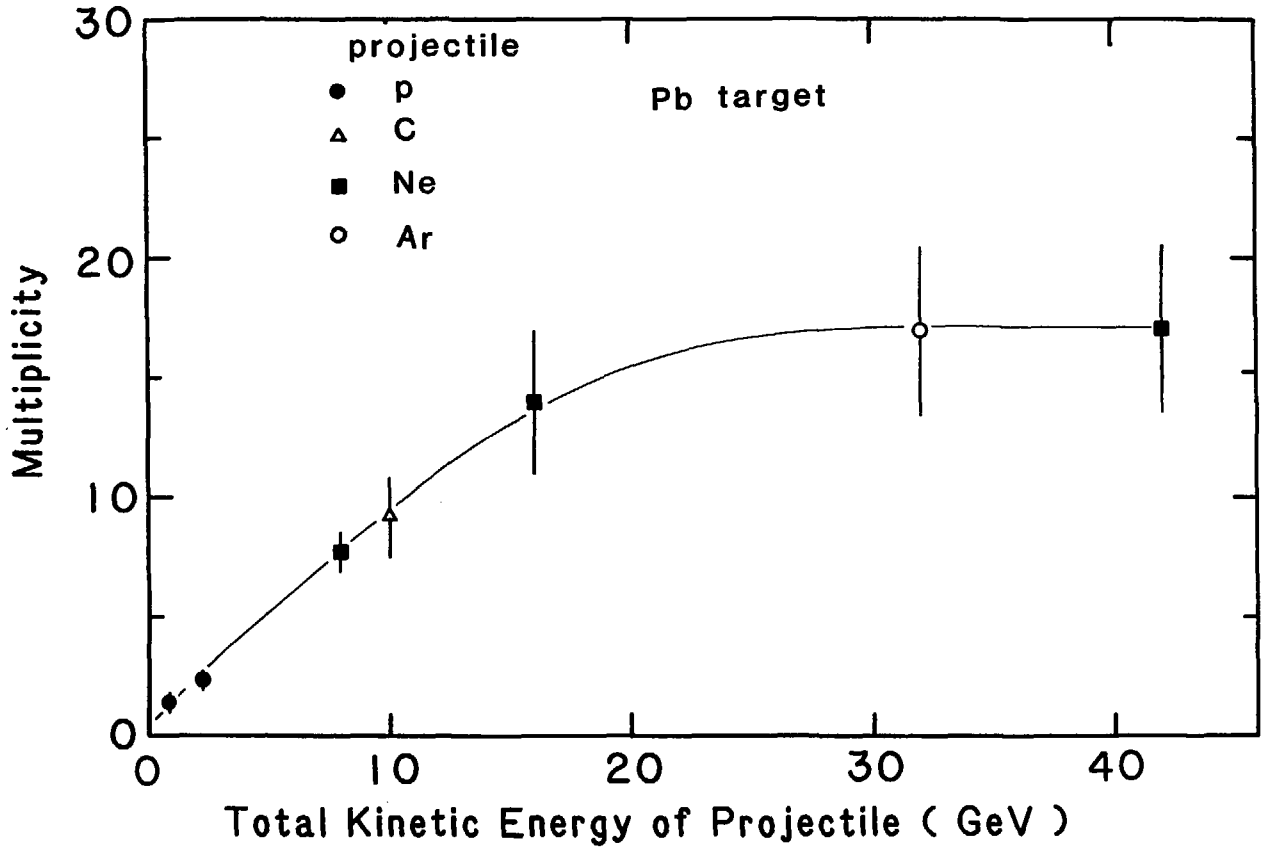
projectile
p
C
Ne
Ar
Pb target
Multiplicity
Total Kinetic Energy of Projectile (GeV)
0
10
20
30
40

Fig. 6

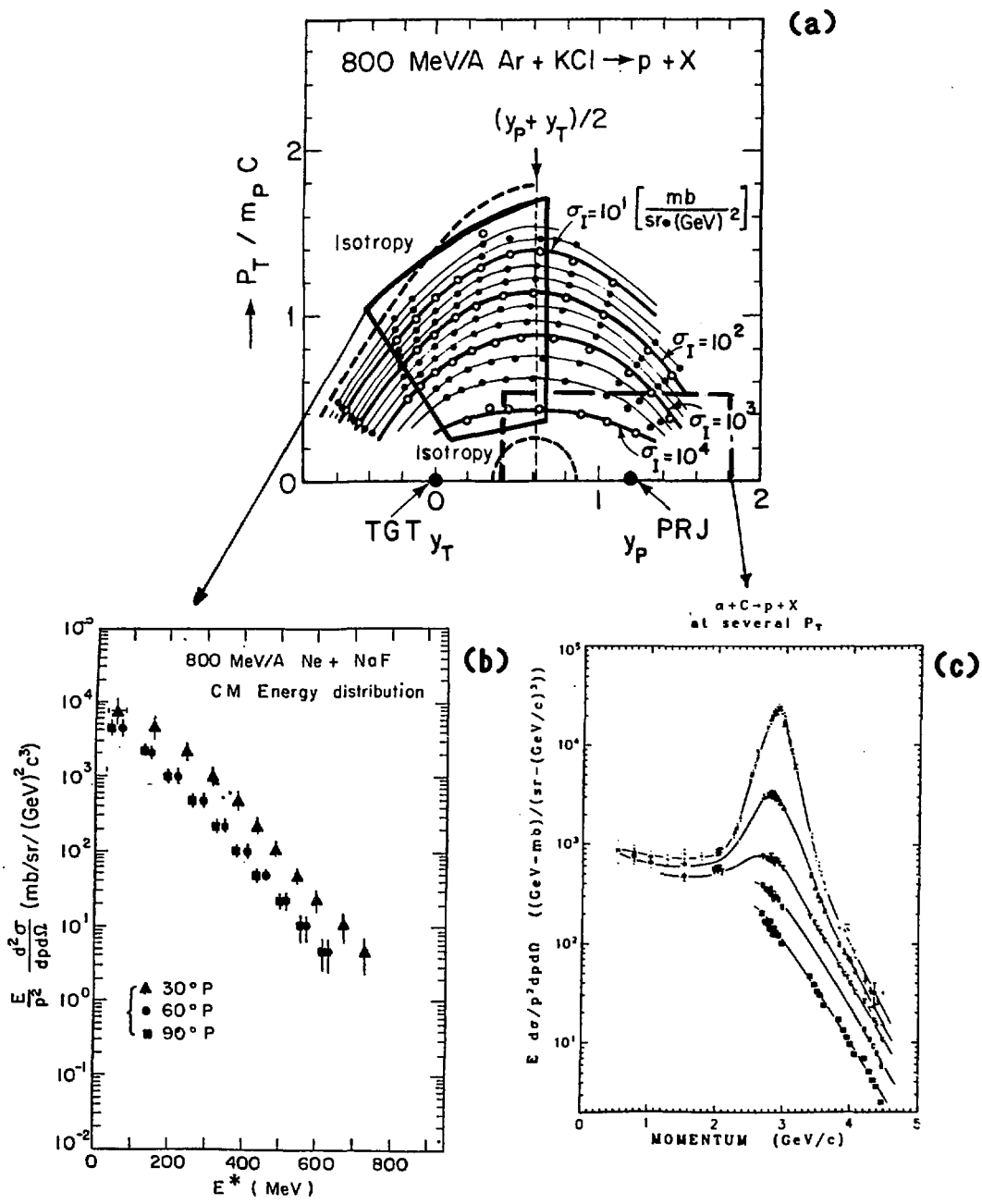
(a)
800 MeV/A Ar + KCl → p + X
$(y_p + y_T)/2$
$P_T / m_p C$
Isotropy
$\sigma_I = 10^1 \left[\frac{mb}{sr \cdot (GeV)^2}\right]$
$\sigma_I = 10^2$
$\sigma_I = 10^3$
$\sigma_I = 10^4$
Isotropy
TGT y_T
y_p PRJ
(b)
800 MeV/A Ne + NaF
CM Energy distribution
$\frac{E}{p^2}\frac{d^2\sigma}{dpd\Omega}$ (mb/sr/(GeV)^{2}c^3)
30° P
60° P
90° P
E* (MeV)
(c)
α+C→p+X
at several P_T
E dσ/p²dpdΩ ((GeV-mb)/(sr-(GeV/c)²))
MOMENTUM (GeV/c)

Fig. 7

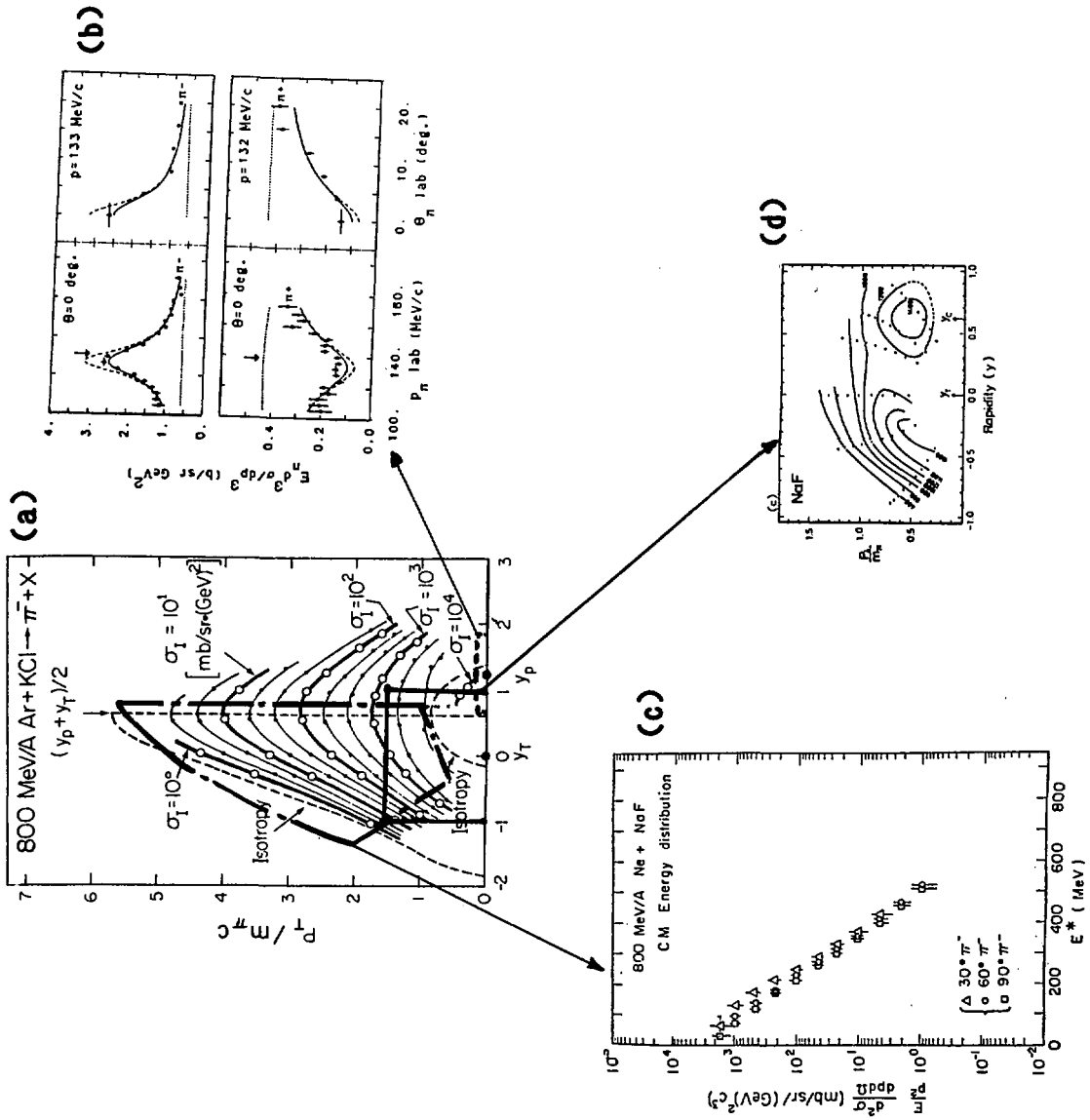
(a)
800 MeV/A Ar+KCl → π⁻+X
(y_p+y_T)/2
σ_I = 10^1 [mb/sr•(GeV/c)³]
σ_I=10^2
σ_I = 10^3
σ_I=10^4
σ_I=10^5
Isotropy
Isotropy
P_T / m_π c
y_p
y_T
(b)
θ=0 deg.
p=133 MeV/c
p=132 MeV/c
π⁻
π⁺
E_n d³σ/dp³ (b/sr GeV²)
p_n lab (MeV/c)
θ_n lab (deg.)
(c)
800 MeV/A Ne + NaF
CM Energy distribution
Δ 30° π⁻
○ 60° π⁻
□ 90° π⁻
E* (MeV)
(d)
NaF
Rapidity (y)

Fig. 8

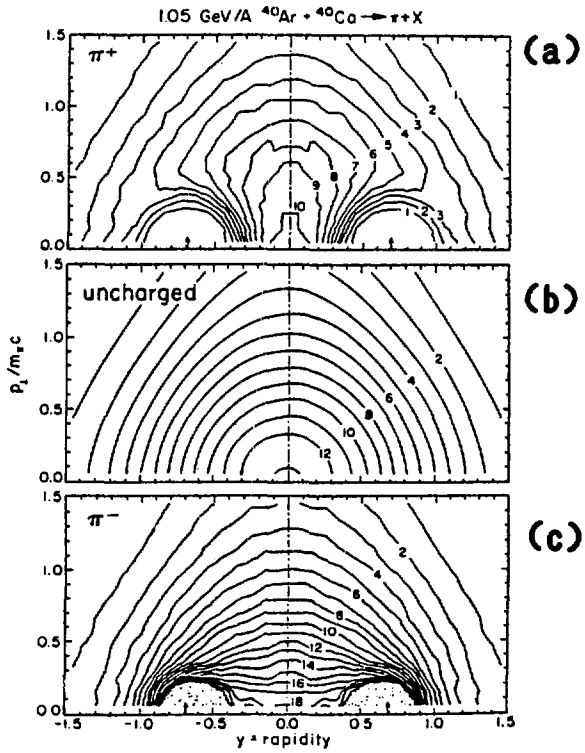
1.05 GeV/A ^{40}Ar + ^{40}Ca → π+X
π+
(a)
uncharged
(b)
π−
(c)
$p_t/m_\pi c$
y = rapidity
-1.5
-1.0
-0.5
0.0
0.5
1.0
1.5
0.0
0.5
1.0
1.5

Fig. 9

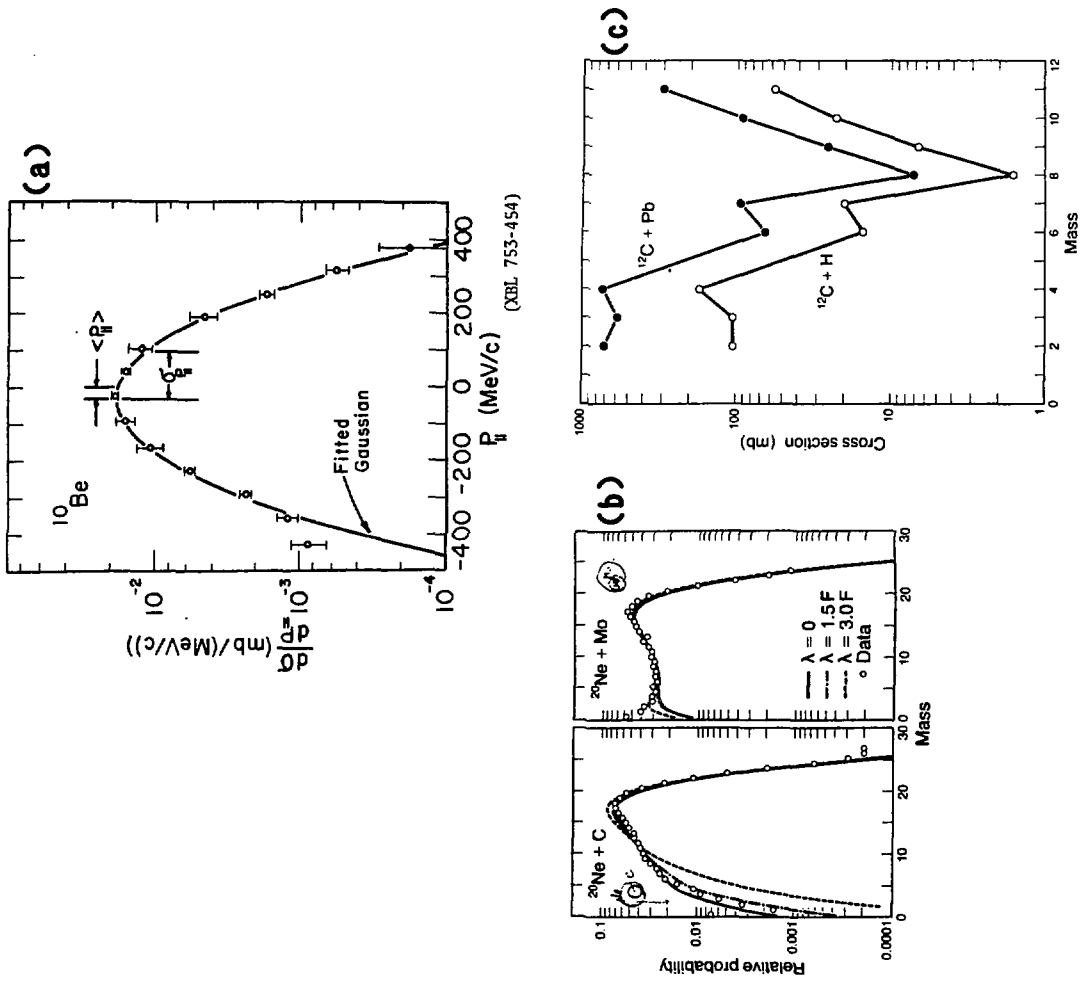
(a)
^{10}Be
Fitted Gaussian
$\frac{d\sigma}{dp_{\parallel}}$ (mb/(MeV/c))
$p_{\parallel}$ (MeV/c)
(XBL 753-454)
(b)
^{20}Ne + C
^{20}Ne + Mo
λ = 0
λ = 1.5F
λ = 3.0F
° Data
Relative probability
Mass
(c)
^{12}C + Pb
^{12}C + H
Cross section (mb)
Mass

Fig. 10

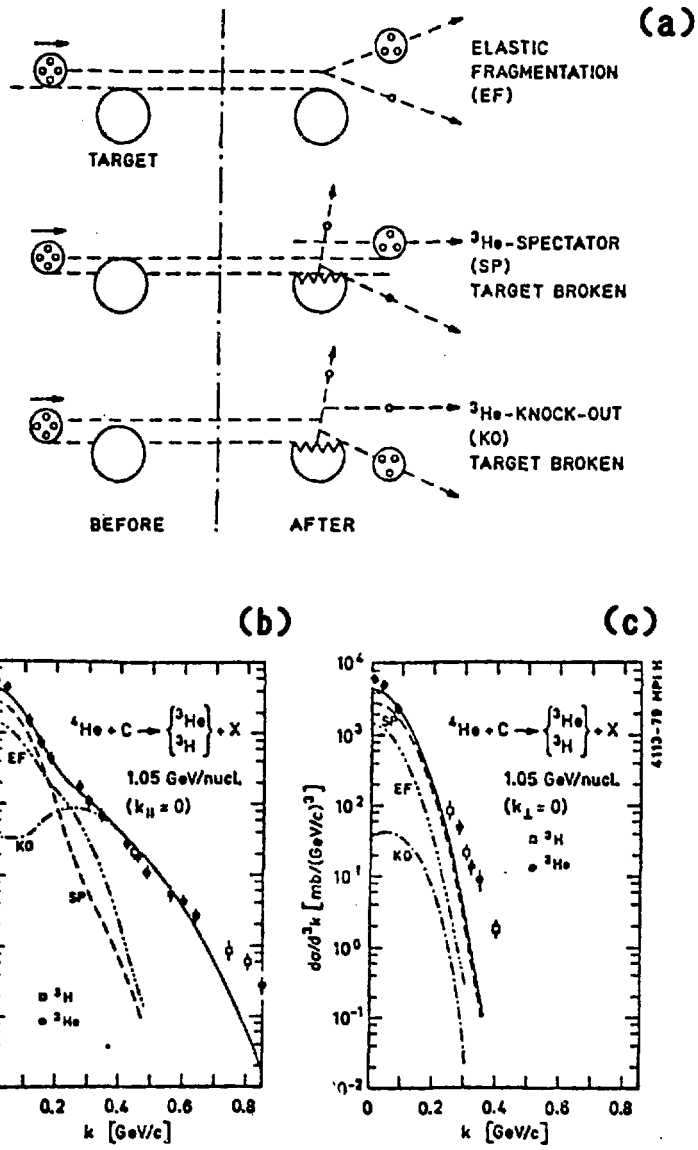
(a)
ELASTIC
FRAGMENTATION
(EF)
TARGET
^{3}He-SPECTATOR
(SP)
TARGET BROKEN
^{3}He-KNOCK-OUT
(KO)
TARGET BROKEN
BEFORE
AFTER
(b)
(c)
^{4}He + C → {^{3}He, ^{3}H} + X
1.05 GeV/nucl.
(k_{II} = 0)
($k_{\perp}$ = 0)
EF
KO
SP
^{3}H
^{3}He
$d\sigma/d^3k$ [mb/(GeV/c)^3]
k [GeV/c]
4113-78 HPI H

Fig. 11

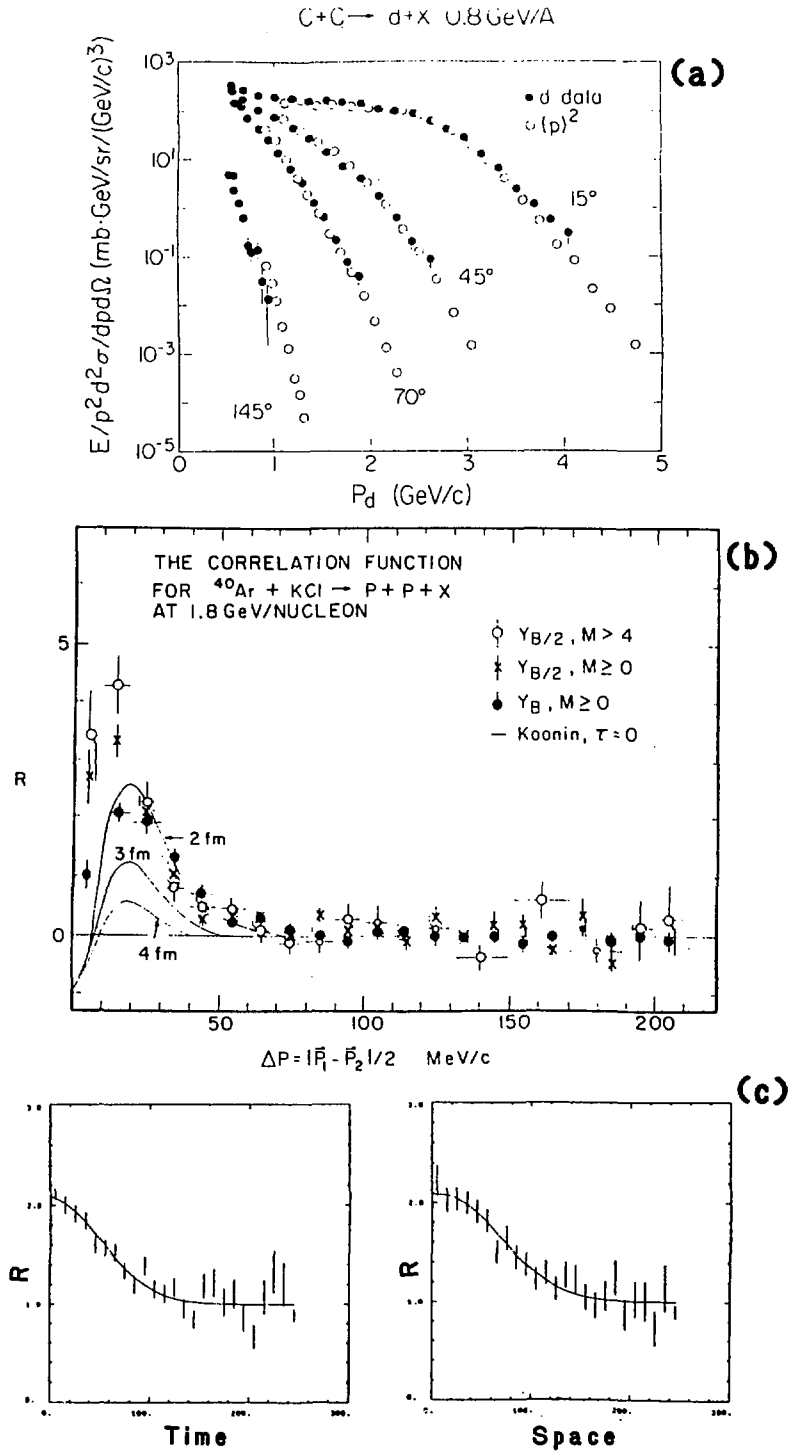
C+C→ d+X 0.8GeV/A
(a)
• d data
○ (p)²
15°
45°
70°
145°
E/p²d²σ/dpdΩ (mb·GeV/sr/(GeV/c)³)
P_d (GeV/c)
(b)
THE CORRELATION FUNCTION
FOR ⁴⁰Ar + KCl → P+P+X
AT 1.8 GeV/NUCLEON
Y_B/2, M > 4
Y_B/2, M ≥ 0
Y_B, M ≥ 0
— Koonin, τ = 0
2 fm
3 fm
4 fm
R
ΔP = |P⃗₁ - P⃗₂|/2 MeV/c
(c)
R
Time
R
Space

Fig. 12

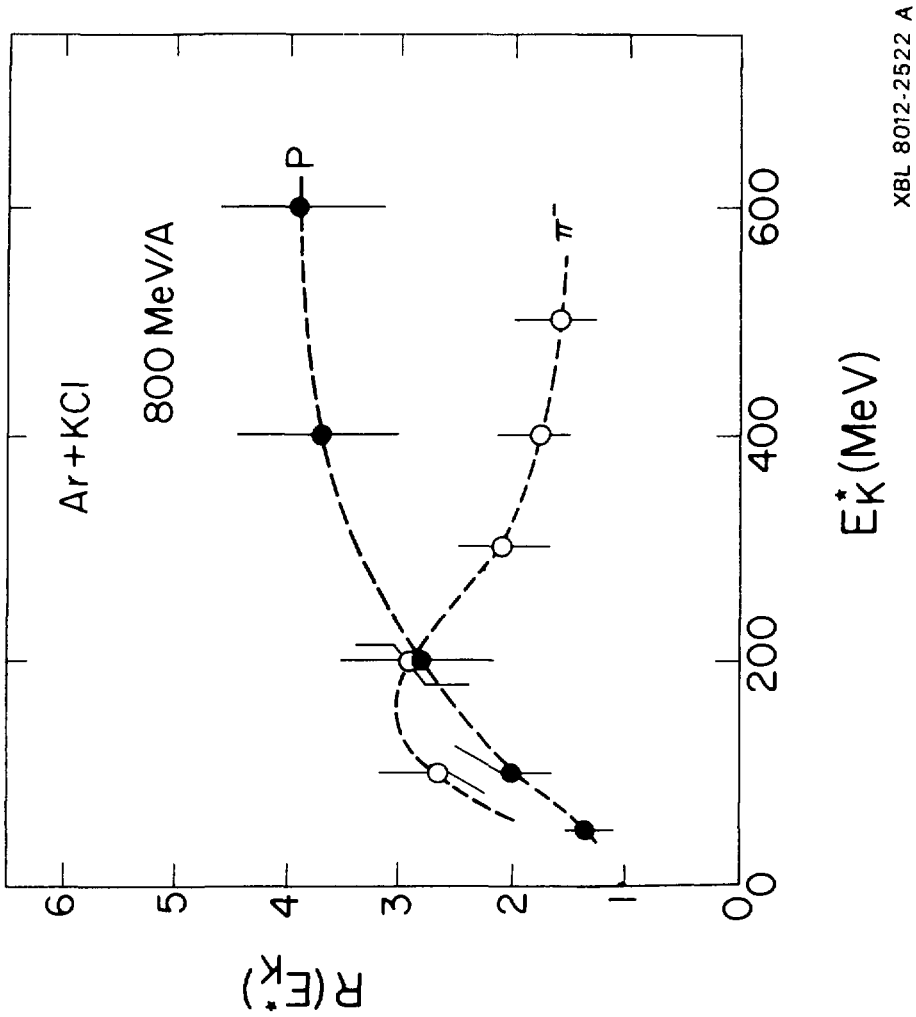
Ar+KCl
800 MeV/A
P
π⁻
R(E*K)
E*K (MeV)
0
200
400
600
1
2
3
4
5
6
XBL 8012-2522 A

Fig. 13

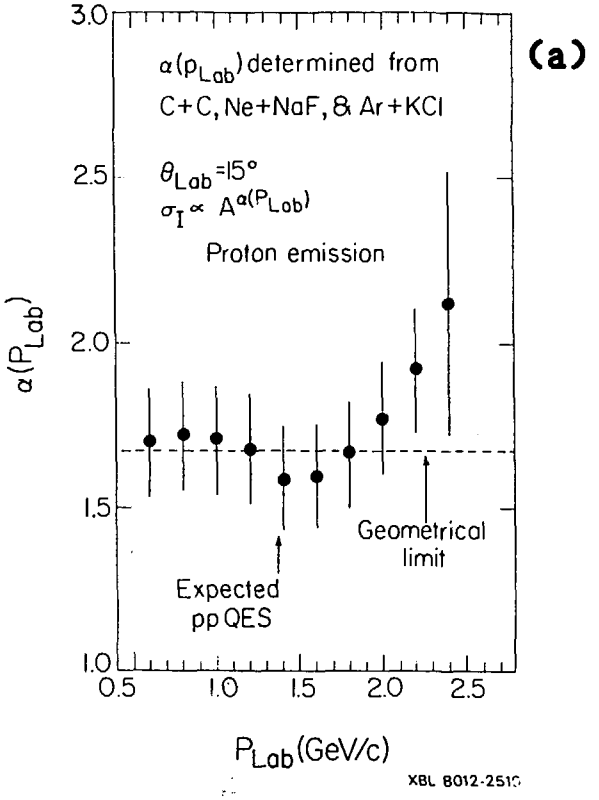
(a)
$\alpha(p_{Lab})$ determined from
C+C, Ne+NaF, & Ar+KCl
θ_{Lab}=15°
$\sigma_I \propto A^{\alpha(P_{Lab})}$
Proton emission
Geometrical limit
Expected pp QES
$\alpha(P_{Lab})$
P_{Lab}(GeV/c)
3.0
2.5
2.0
1.5
1.0
0.5
1.0
1.5
2.0
2.5
XBL 8012-2510

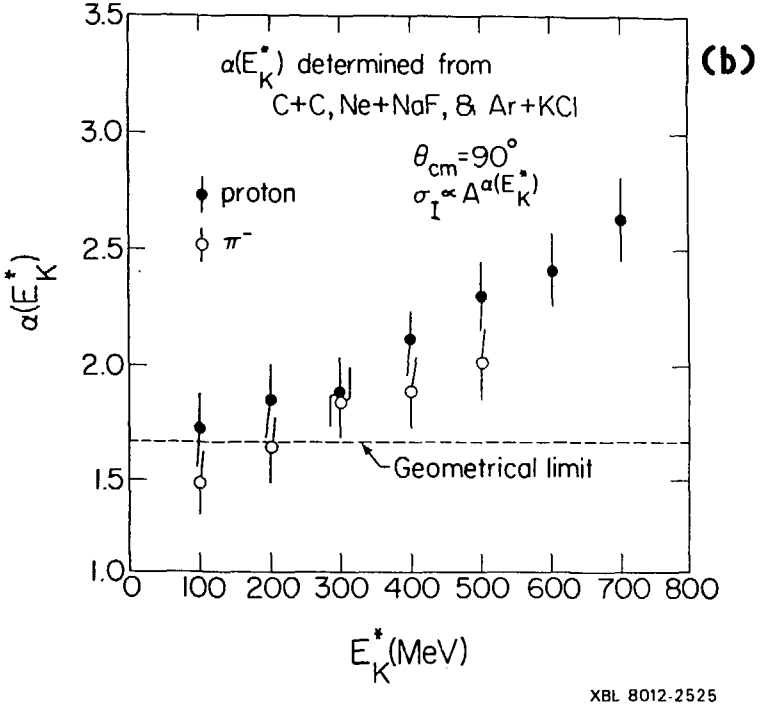
(b)
$\alpha(E_K^*)$ determined from
C+C, Ne+NaF, & Ar+KCl
θ_{cm}=90°
$\sigma_I \propto A^{\alpha(E_K^*)}$
proton
π^-
Geometrical limit
$\alpha(E_K^*)$
E_K^*(MeV)
3.5
3.0
2.5
2.0
1.5
1.0
0
100
200
300
400
500
600
700
800
XBL 8012-2525

Fig. 14

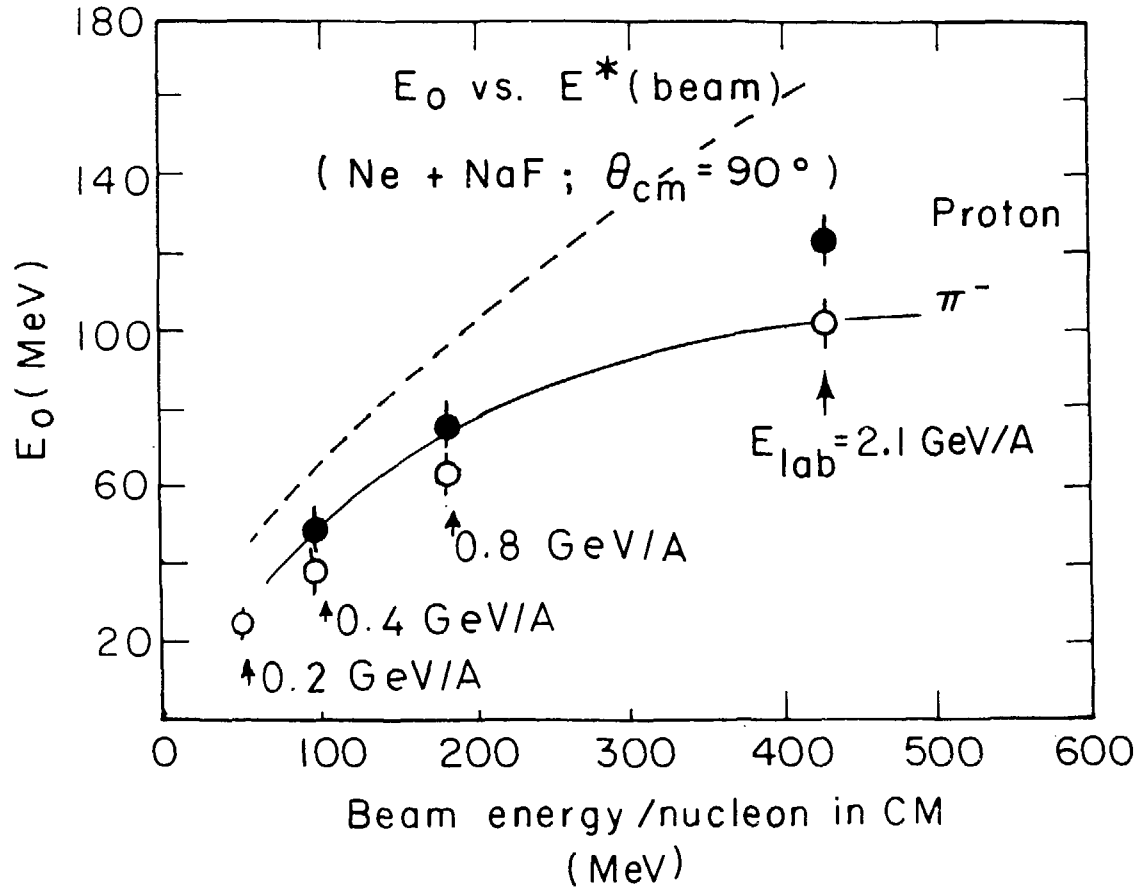
180
140
100
60
20
E_o vs. E^*(beam)
(Ne + NaF ; θ_{cm} = 90°)
Proton
π^-
E_o(MeV)
E_{lab} = 2.1 GeV/A
0.8 GeV/A
0.4 GeV/A
0.2 GeV/A
0
100
200
300
400
500
600
Beam energy /nucleon in CM
(MeV)

Fig. 15

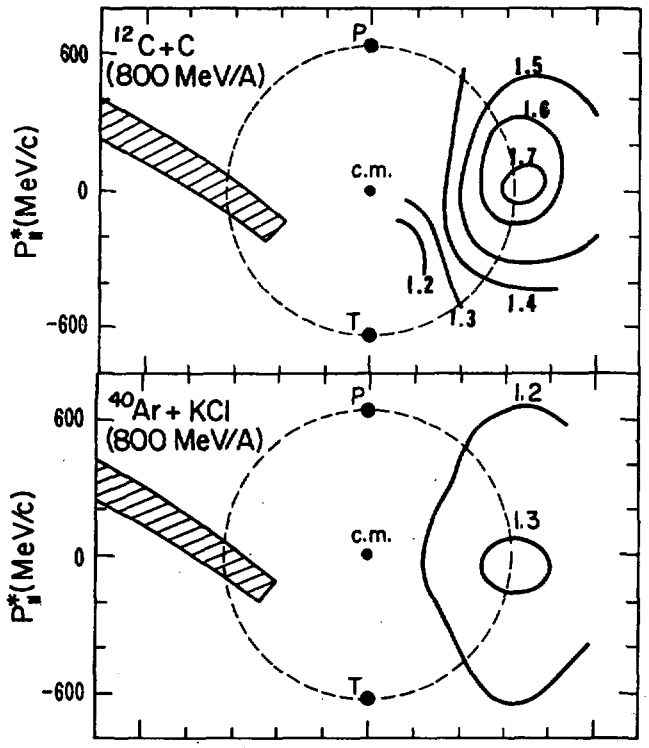
^{12}C+C
(800 MeV/A)
P
c.m.
T
600
0
-600
$P_{\parallel}^{*}$(MeV/c)
1.2
1.3
1.4
1.5
1.6
1.7
^{40}Ar + KCl
(800 MeV/A)
P
c.m.
T
600
0
-600
$P_{\parallel}^{*}$(MeV/c)
1.2
1.3

Fig. 16

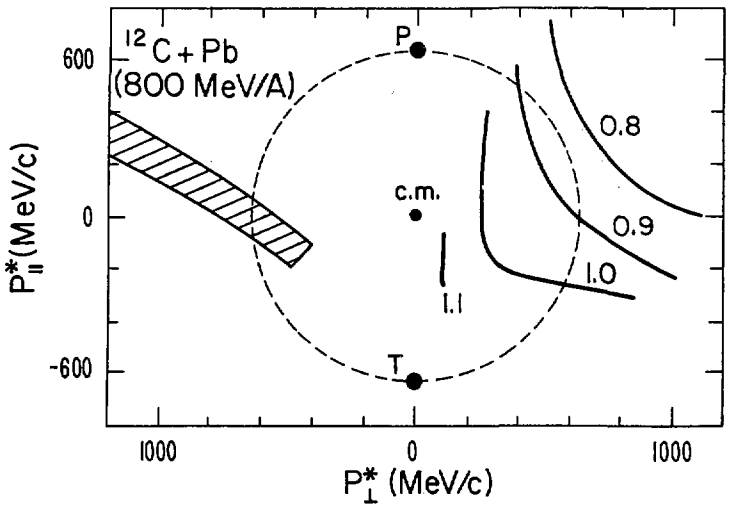

XBL 793-758A

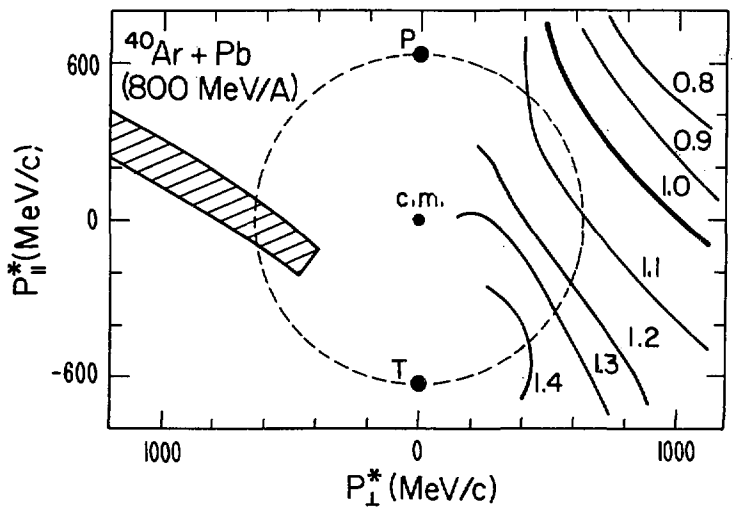

XBL 793-762

Fig. 17

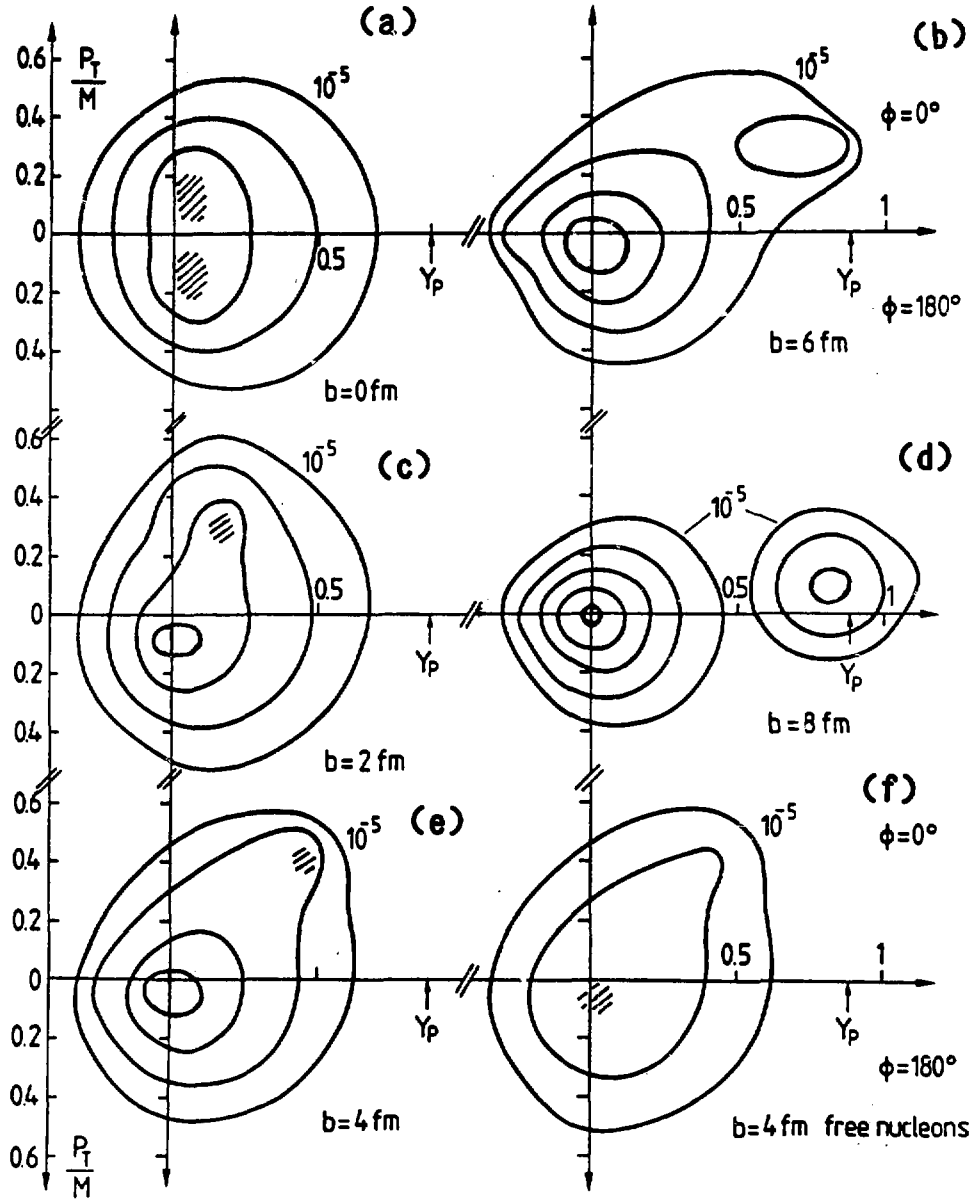
(a)
(b)
(c)
(d)
(e)
(f)
$\frac{P_T}{M}$
10^{-5}
0.5
1
Y_P
$\phi=0°$
$\phi=180°$
b=0 fm
b=6 fm
b=2 fm
b=8 fm
b=4 fm
b=4 fm free nucleons
Ne → U E_{LAB} = 393 MeV/n
XBL 8010-12672

Fig. 18

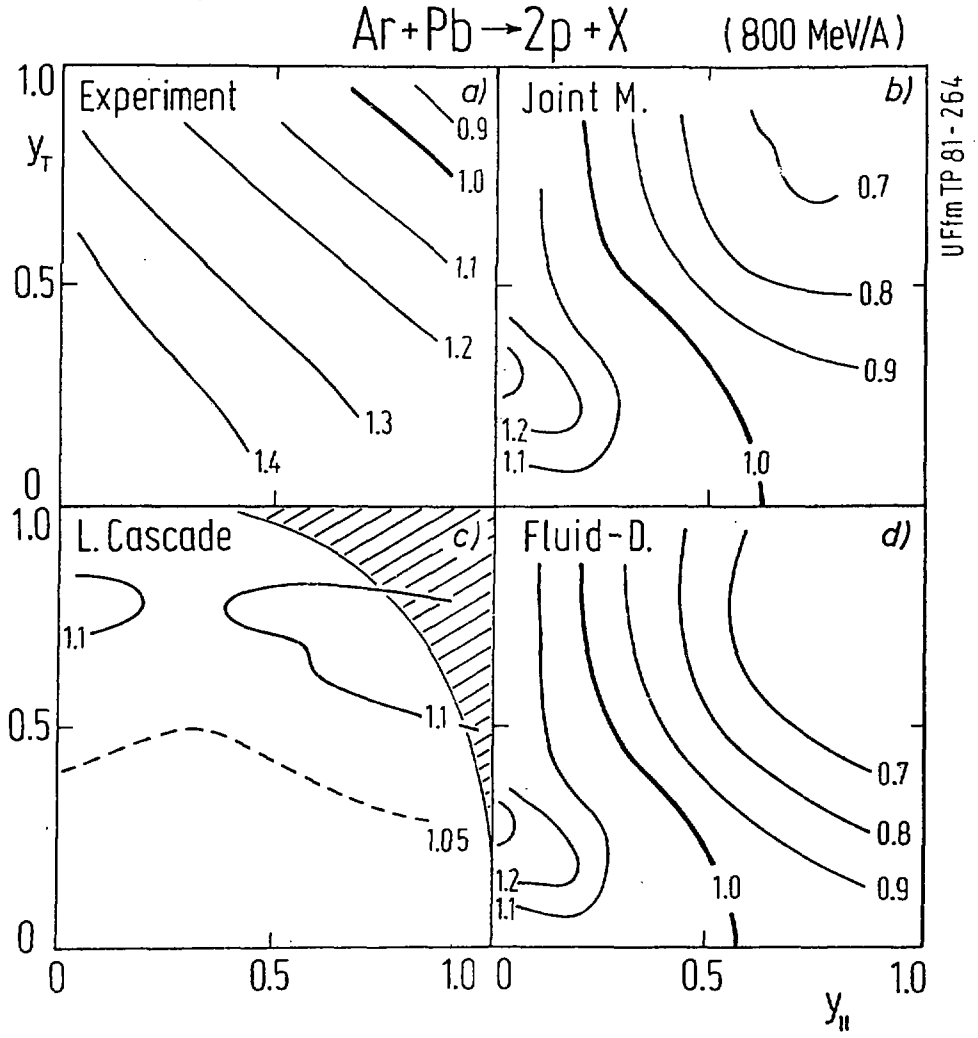
Ar+Pb→2p+X (800 MeV/A)
Experiment
a)
0.9
1.0
1.1
1.2
1.3
1.4
Joint M.
b)
0.7
0.8
0.9
1.0
1.1
1.2
L. Cascade
c)
1.1
1.1
1.05
Fluid-D.
d)
0.7
0.8
0.9
1.0
1.1
1.2
1.0
0.5
0
y_T
y_{II}
UFfm TP 81-264

Fig. 19

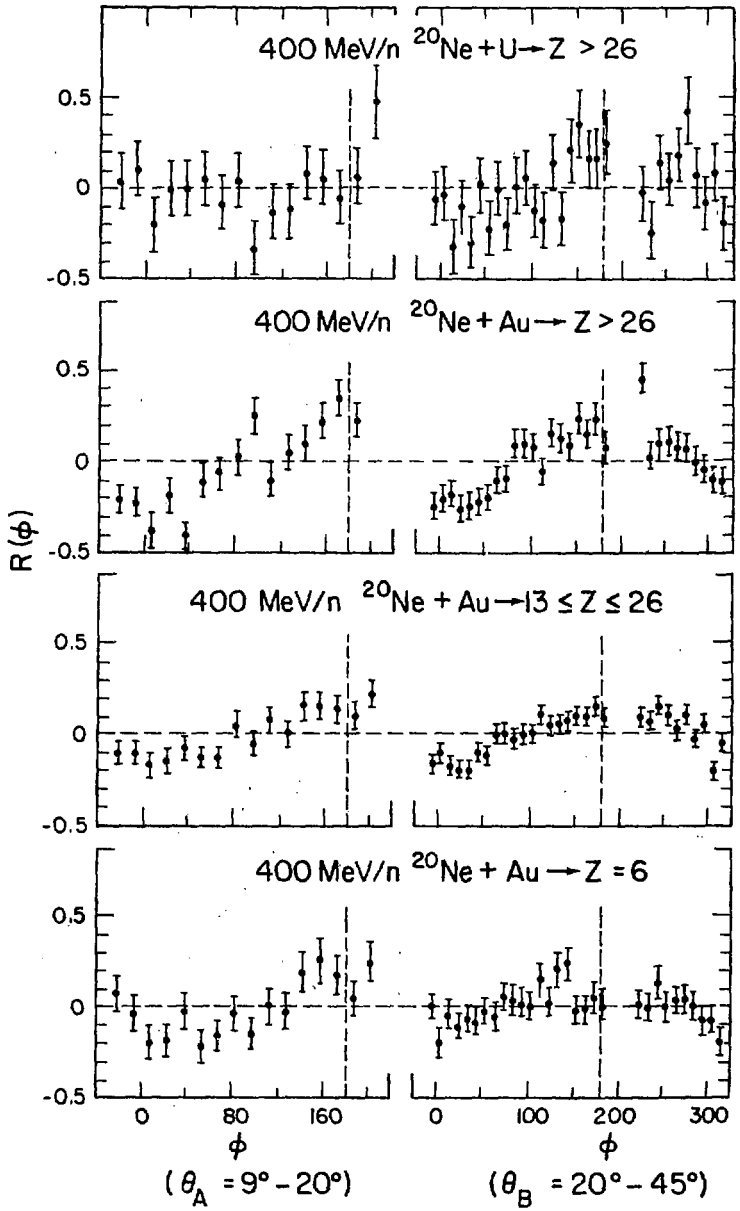
400 MeV/n ^{20}Ne + U → Z > 26
400 MeV/n ^{20}Ne + Au → Z > 26
400 MeV/n ^{20}Ne + Au → 13 ≤ Z ≤ 26
400 MeV/n ^{20}Ne + Au → Z = 6
R(φ)
0.5
0
-0.5
0
80
160
100
200
300
φ
φ
(θ_A = 9° - 20°)
(θ_B = 20° - 45°)

Fig. 20